Effect of thickness disorder on the performance of photonic crystal surface wave sensors

Aleksei Anopchenko,[1,*] Agostino Occhicone,[1] Riccardo Rizzo,[1,2] Alberto Sinibaldi,[1] Giovanni Figliozzi,[1] Norbert Danz,[3] Peter Munzert,[3] and Francesco Michelotti[1]

[1]*Department of Basic and Applied Science for Engineering, Sapienza University of Rome, Via A. Scarpa 16, 00161 Rome, Italy*

[2]*Currently with the Department of Applied Science and Technology, Politecnico di Torino, C.so Duca degli Abruzzi 24, 10129 Torino, Italy*

[3]*Fraunhofer Institute for Applied Optics and Precision Engineering IOF, Albert-Einstein-Str. 7, 07745 Jena, Germany*

[*]*oleksiy.anopchenko@uniroma1.it*

Abstract: We investigated experimentally and numerically the robustness of optical sensors based on Bloch waves at the surface of periodic one-dimensional photonic crystals. The distributions of sensor characteristics caused by the fabrication uncertainties in dielectric layer thicknesses have been analyzed and robustness criteria have been set forth and discussed. We show that the performance of the surface wave sensors is sufficiently robust with respect to the changes of the photonic crystal layer thicknesses. Layer thickness optimization of the photonic crystal, carried out to achieve low limit of detection, leads to an improvement of the robustness of the surface wave sensors that is attributed to Bloch states lying deeper in the photonic band gap.

References and links

1. A. Yariv and P. Yeh, *Optical Waves in Crystals: Propagation and Control of Laser Radiation* (Wiley, 1984).
2. A. Farmer, A. C. Friedli, S. M. Wright, and W. M. Robertson, "Biosensing using surface electromagnetic waves in photonic band gap multilayers," Sens. Actuat. B **173**, 79–84 (2012).
3. V. N. Konopsky, T. Karakouz, E. V. Alieva, C. Vicario, S. K. Sekatskii, and G. Dietler, "Photonic crystal biosensor based on optical surface waves," Sensors (Basel) **13**(3), 2566–2578 (2013).
4. P. Rivolo, F. Michelotti, F. Frascella, G. Digregorio, P. Mandracci, L. Dominici, F. Giorgis, and E. Descrovi, "Real time secondary antibody detection by means of silicon-based multilayers sustaining Bloch surface waves," Sens. Actuat. B **161**(1), 1046–1052 (2012).
5. L. B. Yu, E. Barakat, T. Sfez, L. Hvozdara, J. Di Francesco, and H. P. Herzig, "Manipulating Bloch surface waves in 2D: A platform concept-based flat lens," Light Sci. Appl. **3**(1), e124 (2014).
6. E. Descrovi, T. Sfez, M. Quaglio, D. Brunazzo, L. Dominici, F. Michelotti, H. P. Herzig, O. J. F. Martin, and F. Giorgis, "Guided Bloch surface waves on ultrathin polymeric ridges," Nano Lett. **10**(6), 2087–2091 (2010).
7. E. A. Bezus, L. L. Doskolovich, D. A. Bykov, and V. A. Soifer, "Phase modulation of Bloch surface waves with the use of a diffraction microrelief at the boundary of a one-dimensional photonic crystal," JETP Lett. **99**(2), 63–66 (2014).
8. A. P. Vinogradov, A. V. Dorofeenko, A. M. Merzlikin, and A. A. Lisyansky, "Surface states in photonic crystals," Phys.- Usp. **53**(3), 243–256 (2010).
9. H. Raether, *Surface plasmons on smooth and rough surfaces and on gratings* (Springer, 1988).
10. R. Rizzo, N. Danz, F. Michelotti, E. Maillart, A. Anopchenko, and C. Wächter, "Optimization of angularly resolved Bloch surface wave biosensors," Opt. Express **22**(19), 23202–23214 (2014).
11. R. Rizzo, N. Danz, F. Michelotti, P. Munzert, and A. Sinibaldi, "Limit of detection comparison for surface wave biosensors," Proc. SPIE **9141**, 91410P (2014).
12. S. H. Fan, P. R. Villeneuve, and J. D. Joannopoulos, "Theoretical investigation of fabrication-related disorder on the properties of photonic crystals," J. Appl. Phys. **78**(3), 1415–1418 (1995).
13. F. Bragheri, D. Faccio, M. Romagnoli, T. Krauss, and J. Roberts, "Effects of random and systematic perturbations in a one-dimensional photonic crystal wavelength converter," Phys. Rev. E Stat. Nonlin. Soft Matter Phys. **70**(1), 017601 (2004).

14. M. A. Kaliteevski, D. M. Beggs, S. Brand, R. A. Abram, and V. V. Nikolaev, "Statistics of the eigenmodes and optical properties of one-dimensional disordered photonic crystals," Phys. Rev. E Stat. Nonlin. Soft Matter Phys. **73**(5), 056616 (2006).
15. D. Z. Zhang, Z. L. Li, W. Hu, and B. Y. Cheng, "Broad-band optical reflector - an application of light localization in one-dimension," Appl. Phys. Lett. **67**(17), 2431–2432 (1995).
16. L. Pavesi and P. Dubos, "Random porous silicon multilayers: Application to distributed Bragg reflectors and interferential Fabry-Perot filters," Semicond. Sci. Technol. **12**(5), 570–575 (1997).
17. A. Chiasera, F. Scotognella, L. Criante, S. Varas, G. D. Valle, R. Ramponi, and M. Ferrari, "Disorder in photonic structures induced by random layer thickness," Sci. Adv. Mater. **7**(6), 1207–1212 (2015).
18. A. V. Baryshev, A. M. Merzlikin, and M. Inoue, "Efficiency of optical sensing by a plasmonic photonic-crystal slab," J. Phys. D Appl. Phys. **46**(12), 125107 (2013).
19. *http://www.topas.com/*.
20. N. Danz, A. Kick, F. Sonntag, S. Schmieder, B. Hofer, U. Klotzbach, and M. Mertig, "Surface plasmon resonance platform technology for multi-parameter analyses on polymer chips," Eng. Life Sci. **11**(6), 566–572 (2011).
21. P. Munzert, U. Schulz, and N. Kaiser, "Transparent thermoplastic polymers in plasma-assisted coating processes," Surf. Coat. Tech. **174–175**, 1048–1052 (2003).
22. F. Michelotti, A. Sinibaldi, P. Munzert, N. Danz, and E. Descrovi, "Probing losses of dielectric multilayers by means of Bloch surface waves," Opt. Lett. **38**(5), 616–618 (2013).
23. A. A. Greshnov, M. A. Kaliteevski, and R. A. Abram, "Analytical theory of light localization in one-dimensional disordered photonic crystals," Solid State Commun. **158**, 38–45 (2013).
24. A. Sinibaldi, N. Danz, E. Descrovi, P. Munzert, U. Schulz, F. Sonntag, L. Dominici, and F. Michelotti, "Direct comparison of the performance of Bloch surface wave and surface plasmon polariton sensors," Sens. Actuat. B **174**, 292–298 (2012).
25. G. Figliozzi, "Theoretical and experimental study of Bloch waves on photonic crystals for biomolecular recognition applications," Thesis (Sapienza University of Rome, 2011), p. 117.
26. P. Yeh, A. Yariv, and C.-S. Hong, "Electromagnetic propagation in periodic stratified media. I. General theory," J. Opt. Soc. Am. **67**(4), 423–438 (1977).
27. M. Piliarik and J. Homola, "Surface plasmon resonance (SPR) sensors: approaching their limits?" Opt. Express **17**(19), 16505–16517 (2009).
28. A. Sinibaldi, R. Rizzo, G. Figliozzi, E. Descrovi, N. Danz, P. Munzert, A. Anopchenko, and F. Michelotti, "A full ellipsometric approach to optical sensing with Bloch surface waves on photonic crystals," Opt. Express **21**(20), 23331–23344 (2013).
29. R. Rizzo, "Experimental study of photonic crystal biosensors: development of a new optical configuration and procedures for the chemical functionalization of the surfaces," Thesis (Sapienza University of Rome, 2013), p. 87.
30. D. L. Windt, "IMD - Software for modeling the optical properties of multilayer films," Comput. Phys. **12**(4), 360–370 (1998).
31. O. Glushko, R. Meisels, F. Kuchar, and R. Danzer, "Numerical and experimental investigations of surface roughness in 1D photonic crystals," J. Phys. Condens. Matter **20**(45), 454220 (2008).
32. V. N. Konopsky and E. V. Alieva, "Photonic crystal surface waves for optical biosensors," Anal. Chem. **79**(12), 4729–4735 (2007).
33. D. A. Armbruster and T. Pry, "Limit of blank, limit of detection and limit of quantitation," Clin. Biochem. Rev. **29**(Suppl 1), S49–S52 (2008).
34. S. Johnson and J. Joannopoulos, "Block-iterative frequency-domain methods for Maxwell's equations in a planewave basis," Opt. Express **8**(3), 173–190 (2001).
35. http://www.pcbiosensors.com/.

1. Introduction

Electromagnetic surface waves guided at the boundary between a truncated one-dimensional (1D) photonic crystal (PhC) and an external homogeneous dielectric medium [1], also known as Bloch surface waves (BSW), are used in biosensing [2–4] and photonic devices [5–7]. Differently from electromagnetic waves at the surface of metal layers, surface plasmon polaritons (SPP), BSW are localized at the boundary by Bragg and total internal reflection (TIR) in the PhC and homogeneous medium sides, respectively [8]. Similar to SPP, their field envelope decays exponentially both inside the PhC and the homogeneous medium and they can be excited by prism coupling in the Kretschmann–Raether configuration [9]. Under TIR conditions, BSW may be revealed by a very narrow dip in the angular reflectance spectrum, whose angular position depends on surface perturbations and is used, for example, as a probe of molecular binding events at the PhC surface.

1D PhCs are fabricated by multilayer (ML) deposition of high and low refractive index (RI) layers. The ML geometry offers, on one-side, options to design and optimize PhCs for specific applications [10, 11]. On the other side, ML deposition is subject to fabrication tolerances and uncertainty in the ML thicknesses, which might have a negative impact on performance of the biosensors and photonic devices.

PhCs are fairly robust and tolerant to significant amount of deviation from the designed structure [12–14]. The fabrication-related disorder alters the size of the photonic band gap (PBG). It was shown in [12] that the size of the PBG of a three-dimensional PhC is reduced by structural deviations from the perfect structure. The PhC with a combination of several types of disorder of a certain magnitude (8-20%) retains a PBG width of 13.3% of the original width [12]. A threshold level of disorder in 1D PhCs has been found in [14]: $\sigma = \sigma_{th} \approx (\Delta\omega / \omega_c / 3)^{1/2}$, where σ is the width of a Gaussian distribution of the optical lengths of the PhC period, $\Delta\omega$ is the PBG, and ω_c is the PBG central frequency. Below the threshold the PBG is stable in the presence of the disorder and the density of states in the center of the PBG vanishes [14]. On the contrary, an increase of the PBG has been observed in disordered 1D quarter-wave PhCs [15–17]. For example, a decrease of 30% in light transmission of Ta_2O_5/SiO_2 stack in the range 350-1200 nm is measured in [17] due to a random variation of layer thicknesses (± 20% of the periodic PhC).

The BSW modes, being located in the PBG, may be affected by the structural disorder. Several authors stated that BSW structures are potentially mechanically robust and tolerant against fabrication and measurement errors [2, 5, 18]. However, there are no reports that discuss the robustness to fabrication tolerance quantitatively. Such tolerance analysis is essential because it enables manufacturing and optimization of robust BSW biosensors and photonic devices.

In this work, we analyze the dependence of the BSW resonance depth, width, sensitivity, and limit of detection (LoD) on the fabrication uncertainty in ML thicknesses. To achieve a low LoD it is necessary to operate the BSW sensor in a narrow angular range [10], so that the uncertainties, which lead to an angular shift or shape deviations of the BSW resonance, have to be minimized. We define robustness of the BSW sensor as its ability to maintain a certain resonance angle and LoD value upon changes in the ML thicknesses due to fabrication errors. We will show that BSW sensors with an optimized PhC design, besides having an enhanced sensitivity and LoD, are also more robust against fabrication tolerances. Even though our robustness analysis will be limited to the BSW sensors, it could also be extended to other photonic devices based on electromagnetic surface waves.

2. Experimental and numerical techniques

The 1D PhCs used in the present work are fabricated by plasma ion assisted electron beam evaporation (PIAD) of inorganic dielectric layers under high vacuum conditions (3×10^{-4} mbar) using an APS904 coating system (Leybold Optics). Because of the possibility to deposit coatings with an adjustable densification and stoichiometry at low substrate temperature (< 100 °C) the PIAD is suitable for the deposition of the PhCs on plastic substrates, which are of importance for disposable biochips. Plastic substrates made of a cyclic olefin copolymer (TOPAS 5013/6013) are used in this work [19], which also serve as a tool to excite the BSW. They include molded cylindrical micro-lenses that permit to operate in the attenuated total internal reflection and to collimate the reflected light (Fig. 1) [20].

After initial cleaning, the plastic substrates were preconditioned by plasma etching with the APS plasma source and low ion energies for 60 s. The 1D PhC is formed by alternating evaporation of the high-RI layers of tantalum oxide (Ta_2O_5) and low-RI silica (SiO_2) layers. The deposition rates were 0.25 nm/s and 0.5 nm/s for Ta_2O_5 and SiO_2, respectively. In order to achieve low internal stress levels and absorption losses in the deposited films, a medium level argon ion assistance with ion energies of about 80 eV was applied [21]. The 1D PhC has four pairs of Ta_2O_5 and SiO_2 layers with the thicknesses of d_H = 170 nm and d_L = 495 nm,

respectively. An additional SiO_2 layer was deposited onto the substrate first to improve the reliability of the ML stack. So that, the first and the last layer in the ML stack are SiO_2 layers. A quartz crystal oscillator was used for thickness monitoring during the deposition of the PhC.

A large number of the polymeric substrates can be coated with the PhC in one deposition run in our coating plant. The number depends on the size of the polymeric substrates, the size of the coating chamber, and the substrate holder geometry. Currently we are able to deposit 200 sensor chips per batch, but this number could be scaled up to 480 chips/batch when working with an optimized substrate holder configuration. Using a deposition plant with a larger coating chamber and an optimized substrate holder concept would further increase this number.
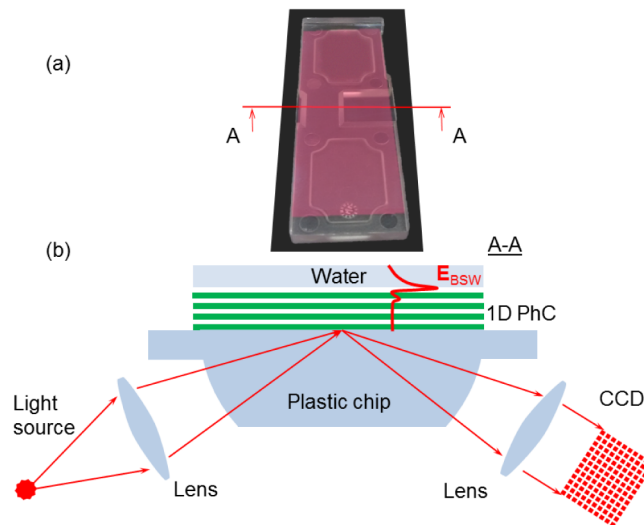

Fig. 1. (a) A false-color image of the TOPAS plastic chip with the Ta_2O_5/SiO_2 1D PhC deposited onto the chip surface. The PhC appears as a pink coloration of the chip surface. (b) Schematic of the chip cross-section along the A-A line and BSW resonance measurements.

A batch-to-batch deposition accuracy of $\pm$ 1% is achievable by the PIAD method with optimal densified layers on glass substrates, and can be attributed to random errors of the thickness monitoring system and the evaporation process itself. In the present case of PhC deposited on polymeric substrates a $\pm$ 3% batch-to-batch deviation is found, that is due to the need of a lower densification level for all layers to prevent cracking and delamination.

For the PhC we used in the experiments reported here, which were deposited in a single batch, we measured an uncertainty of $\pm$ 3% in the layer thicknesses, due to an unfavorable substrate holder configuration. Therefore they are a representative sample of the population of PhC produced in different batches. This $\pm$ 3% deviation value was used for all calculations reported in this study.

The RI were measured by reflectance/transmittance spectroscopy of single layers deposited on reference substrates. The extinction coefficients are too small ($\kappa < 10^{-4}$) to be determined by spectrophotometry. They were obtained by measuring and modelling the BSW reflectivity of reference PhCs in a broad angular range [22]. The 1D PhC has been designed to demonstrate the BSW resonance in water (external medium at the surface of the PhC) at the wavelength of operation $\lambda_0 = 804$ nm. The RI and extinction coefficients of Ta_2O_5 and SiO_2 are ($n_H = 2.051$, $\kappa_H = 2 \times 10^{-5}$) and ($n_L = 1.443$, $\kappa_L = 6 \times 10^{-6}$), respectively, at λ_0. The TOPAS substrate and water RI at λ_0 are $n_s = 1.526$ and $n_{H2O} = 1.328$, respectively.

The RI variations of Ta_2O_5 and SiO_2 layers deposited by the PIAD technique are in the order of $\Delta n_{H,L} \sim 1 \times 10^{-3}$. Therefore the RI relative uncertainty is an order of magnitude below that of the thickness variations. For a reflectivity simulation within a narrow angular range (4 deg), the small disorder of the optical length of single layers can be well modeled by the layer thickness disorder only [23].

Angular reflectivity measurements (Fig. 1) are performed in TE polarization at ambient temperature on a modified Surface Plasmon Resonance (SPR) system developed by the Fraunhofer Institute for Applied Optics and Precision Engineering IOF (Jena, Germany) [20, 24]. The system uses spectrally filtered LED illumination with center wavelength λ_0 and 2.5 nm full spectral width. The illumination beam is focused by the substrate's input cylindrical window to a line on the surface of the chip. After total internal reflection and focusing by the second substrate's cylindrical window, the reflected light is collected by a 1280×960 pixel 8-bit CCD camera. Along the CCD pixel columns the angular spectrum is detected, whereas along the CCD rows the signal coming from different positions along the illumination line is obtained. The angular detection range $A = 4$ deg of the CCD camera spans the angles $\theta \in$ [63.2 deg, 67.2 deg] with respect to the normal of PhC surface. The BSW resonances are measured by placing 30 μl of deionized water on the PhC surface. 15 different spots along the illumination line, each averaging 30 CCD rows (PhC surface area ca. 280 μm), are measured. The spots are separated by 30 CCD rows. Reflectivity curves are normalized to the reflectivity measured in air with no resonance present.

The investigation of the statistical distributions of BSW parameters caused by the fabrication uncertainties are obtained by simulating BSW resonances by means of a custom-built Matlab algorithm [25] based on the transfer matrix method [26]. In the simulations we assume:

- thicknesses of the low and high RI layers deposited by PIAD vary in a range of ± 3% with respect to the designed/original value;

- layer thicknesses change randomly for all layers within the 3% value, i.e., the ML stacks might be aperiodic to a small degree.

Such assumptions are justified for the PIAD deposition of low densification layers using non-optimized substrate holder configuration. It is noteworthy that systematic errors, for example, due to the thickness calibration of density factors, do not affect the validity and generality of the results reported in this work.

As it is commonly done for SPR [27], the limit of detection of the BSW sensor is defined in [10]:

$$LoD_S = \frac{\sigma}{S_S} = \frac{2.8 \times 10^{-3}}{FoM_S} \sqrt{\frac{A}{W \cdot N}}, \tag{1}$$

where σ is the sensor output noise, S_S is surface sensitivity of the sensor, N is the number of pixels of the CCD camera along the direction used for angular detection ($N = 1280$), and FoM is the figure of merit [28]:

$$FoM_S = S_S \frac{D}{W}, \tag{2}$$

where D and W are the depth and full width at half maximum of the angular resonance, respectively. The coefficient of 2.8×10^{-3} in Eq. (1) corresponds to the 8-bit CCD camera [10, 11]. The surface sensitivity S_S is defined as a change of the resonance position upon the addition of biolayer with thickness $t = 1$ nm and $n_{bio} = 1.450$ and given in deg/nm [10].

Instead of surface sensitivity one can make use of the volume sensitivity S_V, i.e. the change of the resonance angle upon a change of the refractive index of the external medium, which is more practical for quick laboratory tests. S_V and S_S are related by the relation:

$$S_V = \frac{d\theta}{dn} = \frac{d\theta}{dt} \cdot \frac{dt}{dn} = S_S \frac{dt}{dn} \approx S_S \frac{L_p}{n_{bio} - n_{H_2O}}, \qquad (3)$$

where L_p is the penetration depth of the evanescent BSW tail in the external medium. Equation (3) is valid for a small thickness of the biolayer. In the present design the penetration depth is $L_p = 220$ nm at λ_0. Consequently the two quantities LoD and FoM defined in the Eqs. (1) and (2) will take different expression and units when being related to bulk RI changes.

3. Results and discussion

Experimental and numerical analysis of BSW resonance distributions

The characteristics of the BSW resonance were studied experimentally. Measured reflectance curves featuring the BSW resonance are shown in Fig. 2(a) for a set of 19 virgin PhCs deposited on plastic substrates. The measurement record starts with the reflectance curve of a bare surface of the PhC. While recording, water droplets are placed on the PhC surface and recording continues for less than half a minute. Measurement intervals are kept short to avoid any non-specific resonance shift, for example due to water penetration into the low density PhC layers [22, 29]. This procedure is repeated for all samples from the same deposition batch. A distribution of the resonance position, depth, and width is clearly observed in Fig. 2(a). The standard deviation of the BSW resonance angle distribution amounts to 165 mdeg. This is primarily due to the variations in the PhC layer thicknesses, which will be shown in the next paragraph.
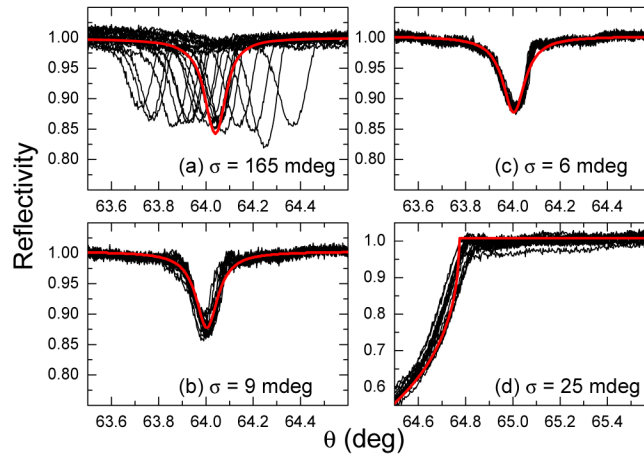

Fig. 2. (a) TE reflectivity curves around the BSW resonance in water for the central spot on 19 virgin PhCs deposited on plastic chips. Thick red curve in (a) is the fit model of the centermost reflectivity curve. (b) BSW resonance distribution due to variations among 15 different spot positions on the surface of one chip. (c) BSW resonance distribution due to the uncertainty of the mechanical fixture. The red curves in (b) and (c) are examples of the Lorentzian fit. (d) The TIR angle measurements from the surface of the TOPAS chip in contact with 1-propanol. The red curve in (d) is an example of the Fresnel's formula fit. Measurements were performed at room temperature with the excitation wavelength centered at λ_0. The standard deviation of the BSW and TIR angular positions are shown in the figures.

The BSW resonance in Fig. 2(a) is shown for the central spot (number 8) at the chip surface. The standard deviation of the BSW resonance angle distribution along the 15 spots is 9 mdeg (Fig. 2(b)). This distribution may be attributed to inhomogeneity of the plastic chip

due to the injection molding process. During the measurement the plastic chip is fixed in the optical system by a mechanical fixture. The uncertainty in the angular position of the BSW resonance due to a possible misalignment of the plastic chip in the fixture is measured to be 6 mdeg (Fig. 2(c)). The angular uncertainty due to the plastic substrates was evaluated by measuring the TIR angle from the surface of the TOPAS chip in contact with 1-propanol (Merck, 100997) using the same measurement setup. The results of TIR measurements are shown in Fig. 2(d). The standard deviation of 25 mdeg is measured for 17 different plastic substrates, which is larger than the standard deviation due to the variations among the different spots (cf. Figure 2(b)).

We point out that all PhC and the liquids used in the experiments were kept at the same ambient temperature, with a maximum fluctuation estimated to be 0.1 °C during the time needed for all measurements. For such fluctuation, the temperature dependence of the RI of either the plastic substrate or water was estimated to give rise at maximum to a change of the resonance angle of 0.7 mdeg, that is much smaller than the uncertainty due to the misalignment of the plastic chip cited above, showing that such temperature fluctuations do not play a role in the investigations reported here.

From the results shown in Fig. 2 we conclude that the uncertainty of the BSW parameters seen in Fig. 2(a) is governed by the variations in the PhC layer thicknesses.

The complex RI of the Ta_2O_5 and SiO_2 layers were obtained by fitting the centermost curve out the 19 (Fig. 2(a)) using a genetic algorithm available in IMD software [30], taking into account the spectral width of the illumination system and allowing the thicknesses of all layers to vary randomly by no more than ± 3% with respect to the design values. The agreement between the experimental and model curves is very good (Fig. 2(a)). The resulting RIs were used to carry out all the numerical simulations that will be discussed in this section. We point out that all the experimental curves shown in Fig. 2(a) can be reproduced by assuming the same values of the complex RI obtained from the centermost curve and simply allowing the thicknesses of all layers to vary within ± 3%, as it will be clarified below.

The RI of silica layers obtained from the fit, $n_L = 1.460$, is slightly larger than that obtained from reflectance/transmittance measurement on single layers cited above. This larger RI is due to water absorption in the low density silica layers [22, 29]. It is noteworthy that the fit model uses the same RI for all SiO_2 layers, despite a possibility of having a non-uniform RI depth profile in the stack. The BSW resonance is not sensitive to the RI changes of the bottom SiO_2 layers because the electric field decays exponentially in the PhC. Similarly the RI of Ta_2O_5 remains unchanged in the fit model because the electric field has nodes in Ta_2O_5 layers.

The BSW resonances are broad and shallow due to the spectral width of the light source and surface roughness of the polymer substrates [24]. The surface roughness scattering might differ from chip to chip, but in our analysis we assume it has a constant value, which we model by an increased extinction in the top silica layer ($\kappa_L^{top} = 8.8 \times 10^{-4}$). It was shown in [31] that the PBG of 1D PhC is almost unaffected by the surface roughness.

For further analysis of the experimental data, the resonances obtained for the 19 samples (spot 8) have been fitted with a three parameter (θ, D, W) Lorentzian function. Here we restrict the investigation to θ, D, W, that contribute to the definition of the LoD, without further consideration of possible PhC geometries that correspond to each measured curve.

The distributions of the parameters extracted from the Lorentzian fits are shown in Fig. 3 (bottom graphs). The values are the average over 7 subsequent reflectance curves taken every second. From the histograms we found the median value (μ) and standard deviation (σ) which are listed in Table 1, together with their ratio (in %).
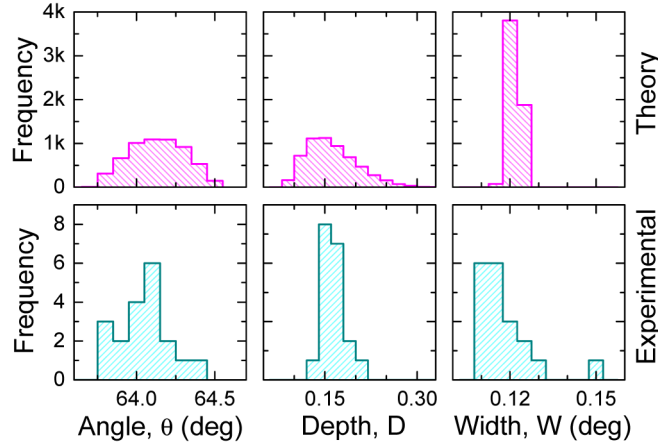
Fig. 3. Histograms of the distributions of simulated (top row) and experimental (bottom row) BSW resonance parameters (experimental data are from Fig. 2(a)). The parameters of experimental resonances have been extracted from Lorentzian fits. An error of ± 3% in the original layer thicknesses is used in the BSW simulations. Spectral broadening of 2.5 nm of the light source and the dispersion of the RI have been taken into account. The histograms are based on sets of 5760 (simulation) and 19 (experiment) sensors.

The experimental histograms are compared to the distributions of θ, D, and W parameters obtained by simulating the BSW resonance of the PhC with the fabrication error of ± 3% in the original layer thicknesses (Fig. 3, top graphs). In the simulations we used the RI extracted from the fit of the centermost experimental curve, namely $n_L = 1.460$, $\kappa_L^{top} = 8.8 \times 10^{-4}$, and we assumed spectral broadening of 2.5 nm of the light source. The dispersion of the RI has also been taken into account. From the histograms of the numerical results we again find the values for μ, σ and σ/μ and listed them in Table 1.

The experimental and numerical median values are consistent for all three parameters, with a slightly larger deviation for W and D which can be due to the difference of the BSW resonance curve from the analytical Lorentzian function used in the fit.

The standard deviations of the angular position (θ) of the BSW resonance for both experimental and simulated distributions are in a good agreement, cf. $\sigma_{exp} = 0.16$ deg and $\sigma_{sim} = 0.17$ deg. It is important to notice that such σ value for the resonance position θ must be smaller than the angular range of the sensor, indicating that, once the sensor has been designed, it is robust with respect to fabrication tolerances. We will discuss this in greater details in the next section.

There are some differences between the experimental and simulated standard deviations ($\sigma_{W, D}$) of the W and D distributions. The largest difference is found for σ_W, whose numerically simulated value is notably smaller than that found experimentally (factor 5). This indicates other effects increasing σ_W that have not been considered in the simulations yet, i.e. the uncertainty and dispersion of material losses and the dependence of W on diffuse light scattering which can vary from sample to sample due to the local quality of the plastic substrates. In the simulations the light scattering is taken into account by assuming a larger extinction coefficient in the top silica layer (κ_L^{top}). However, such coefficient is kept constant in the simulations whereas experimentally it can vary from sample to sample. As far as σ_D is concerned, the value found numerically is larger than the experimental one (factor 2.5). This conforms to a general behavior observed in all our numerical simulations, i.e., for broad resonances, σ_W and σ_D are varying inversely. The experimental relative standard deviations (σ/μ) of D and W are 11.3% and 8.77%, respectively, which are larger than the ± 3% uncertainty of the layers thicknesses. These enlarged uncertainties of D and W in combination with the uncertainty of sensor sensitivity may stretch the uncertainty of the LoD.

Table 1. Median value (µ), standard deviation (σ), and relative error of the BSW resonance parameter distributions

	Experimental distributions			Simulated distributions		
	µ	σ	σ / µ [%]	µ	σ	σ / µ [%]
θ [deg]	64.01	0.16	0.26	64.08	0.17	0.27
W [deg]	0.114	0.010	8.77	0.119	0.002	1.68
D	0.151	0.017	11.3	0.146	0.041	28.1

In Fig. 4 we report the simulated distributions of the volume sensitivity S_V and the related LoD_V. They are calculated numerically using the same procedure we used to evaluate the distributions of θ, *W* and *D*. The median S_V is 18.7 deg/RIU and the standard deviation is ± 0.8 deg/RIU, which corresponds to a surface sensitivity S_S of (0.0129 ± 0.0003) deg/nm. S_V was measured for one in the 19 sensors and equals to 19.5 deg/RIU [11], which agrees well with the simulated median value. Using the measured S_V and noise values, we evaluate the experimental LoD_V value of 1.9×10^{-5} RIU [11], which agrees well with the median value of the broad LoD_V distribution obtained from the simulations (Fig. 4).
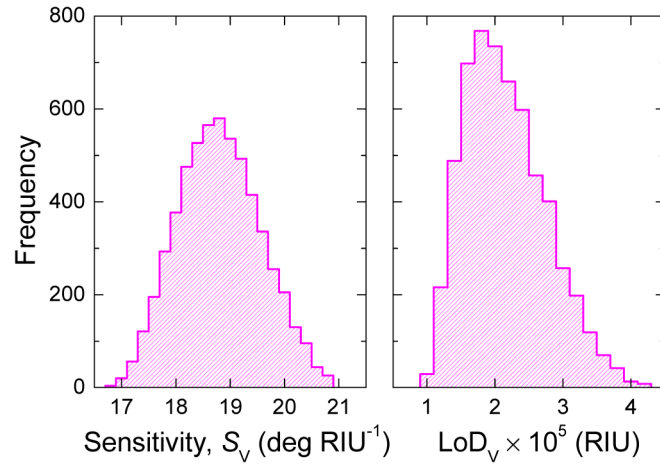

Fig. 4. Simulated histograms of the distributions of S_V and LoD_V simulated for the PhC with an error of ± 3% in the layer thicknesses. Spectral broadening of 2.5 nm of the light source and the dispersion of the RI have been taken into account. The histograms are based on a set of 5760 sensors.

Robustness criteria for the BSW biosensor

The analysis of the reflectance resonance distributions reported above allows us to quantify the robustness of the BSW sensors. On one hand, a robust BSW sensor is characterized by a certain degree of uncertainty of the resonance parameters (e.g., resonance width, depth, etc.), and hence the FoM and LoD, with respect to the degree of ML thickness inhomogeneity. On the other hand, the robustness of the BSW sensor should take into account the uncertainties of the resonance angle, sensitivity, and the angular range of the sensor. For example, as found from Table 1, ± 3% of uncertainty of the layer thicknesses results in < 0.3% of uncertainty of the resonance angle. Therefore, a robust BSW sensor has to satisfy several criteria for either the FoM or the LoD and for the angular resonance position:

    i. Position criterion,

$$\theta - \sigma_\theta \geq \theta_1 > \theta_c, \tag{4}$$

where θ is the designed angle of the BSW resonance of the sensor without an analyte at a given wavelength, σ_θ is the standard deviation of the angular resonance position due to the fabrication tolerances (Table 1), θ_1 is the minimum angle of the available measurement interval (θ_1, θ_2), and θ_c is the TIR angle.

ii. Angular range criterion,

$$\theta + \sigma_\theta + \left(S_S + \sigma_{Ss}\right) \cdot \Delta t_{bio} + \left(S_V + \sigma_{Sv}\right) \cdot \Delta n_{sol} \leq \theta_1 + A = \theta_2, \tag{5}$$

where we took into account that the resonance can shift due to either the formation of a bio-layer at the sensor surface or to a change of the analyte RI. Other contributions could be considered too but are neglected here for the sake of simplicity. Here Δt_{bio} is the maximum thickness of the bio-layer formed during sensor operation, σ_{Ss} and σ_{Sv} are the uncertainties of the surface and volume sensitivities, respectively, due to the fabrication tolerances, Δn_{sol} is the expected RI dynamic range of the solutions during operation. Introducing the Eq. (1) in the Eq. (2) we find that:

$$\theta_1 + 2\sigma_\theta + \left(S_S + \sigma_{Ss}\right) \cdot \Delta t_{bio} + \left(S_V + \sigma_{Sv}\right) \cdot \Delta n_{sol} \leq \theta_1 + A, \tag{6}$$

Therefore the angular range A must be chosen according to:

$$A \geq 2\sigma_\theta + \left(S_S + \sigma_{Ss}\right) \cdot \Delta t_{bio} + \left(S_V + \sigma_{Sv}\right) \cdot \Delta n_{sol} \tag{7}$$

Assuming that practical biosensors are designed to target small analyte concentrations we usually have that $(S_S + \sigma_{Ss}) \cdot \Delta t_{bio} << (S_V + \sigma_{Sv}) \cdot \Delta n_{sol}$ (see for example Table 2 in the next section and [32]) and so that A can be approximated by:

$$A \geq 2\sigma_\theta + \left(S_V + \sigma_{Sv}\right) \cdot \Delta n_{sol} \tag{8}$$

Given that for the experiments reported here $2 \cdot \sigma_\theta \approx 0.3$ deg and, as it will be shown below, $(S_V + \sigma_{Sv}) \sim 20$ deg/RIU and that in practical instruments $\Delta n_{sol} = 0.03$ RIU we have that $A \geq 0.9$ deg for the sensor to be robust against $\pm$ 3% of fabrication tolerances. If one would chose $A = (S_V + \sigma_{Sv}) \cdot \Delta n_{sol} = 0.6$ deg, then the sensor could still operate but only for the designed PhC. Therefore the 4 deg angular range used in the experiments reported here guarantees this robustness criterion but does not optimize the LoD.

iii. Performance criterion,

$$\mu_{LoD} + 1.645 \cdot \sigma_{LoD} \leq LoD^*, \tag{9}$$

where μ_{LoD} is the median LoD value, σ_{LoD} is the LoD uncertainty due to the fabrication tolerances, LoD* is a target LoD, and the factor 1.645 accounts for the 95% confidence limit [33]. This performance criterion may be also written in the following form: $\mu_{FoM} - \sigma_{FoM} \geq FoM^*$. It depends on the BSW optimization choice [10] which out of these two forms to choose.

The angular range criterion shows that the uncertainties of both the angular resonance position and the sensitivity have to be as small as possible in order to have the smallest possible angular range of the sensor and hence to achieve the lowest limit of detection. Given the angular range used ($A = 4$ deg) the position and range criteria are satisfied for the BSW sensor presented above (Fig. 2). The performance criterion is satisfied too, and hence *the BSW sensor is robust*, if the target $LoD_V^* = 3 \times 10^{-5}$ RIU ($LoD_S^* = 44$ pm).

The LoD value found above is large for practical use in biosensing. Reducing *A* below 4 deg down to the limit of 0.9 deg derived above can decrease the LoD by a factor of 2 (see Eq. (1)). Further decrease in *A* will compromise the robustness of the sensor. LoD/FoM optimization can be however performed by changing the PhC geometry. The optimization, in turn, affects the BSW parameter distributions and robustness of the biosensor (see, for example, the performance criterion above). This will be discussed in the next section.

Optimization of the BSW sensor and robustness analysis

The geometry of the BSW sensor described above is not optimized to provide the largest FoM (smallest LoD) at λ_0. To improve the performance, we optimized the sensor by varying the thicknesses of silica and tantalum oxide layers in a broad range of ± 40% (keeping the periodicity of the stack) and assuming a monochromatic illumination at λ_0, i.e., without the 2.5 nm spectral width [10].

We used the nominal values of the refractive indices of the layers given in Section 2. This makes that the BSW resonance angle and the sensitivities are slightly changed with respect to the values found experimentally. Such changes do not affect the general validity of the results we shall describe below.
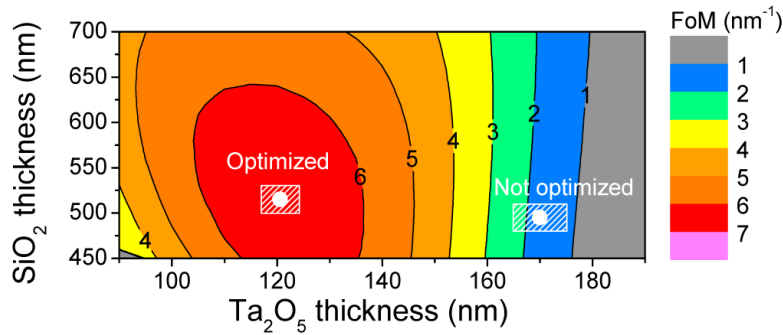

Fig. 5. Dependence of the FoM_S on low and high RI layer thicknesses calculated for the periodic BSW stack with four periods. The value of FoM_S is shown at the contour lines and the color scale bar. Layer thicknesses for the original and optimized BSW stacks are marked by full circles. The layer thickness variations of ± 3% are shown by the white rectangles. The FoM_S optimization has been performed using monochromatic illumination at λ_0.

Figure 5 shows the result of FoM_S optimization for the periodic BSW stack as a function of both low and high RI layer thicknesses. The optimum PhC has been found to have the following thicknesses: 515.0 nm and 120.6 nm for silica and tantalum oxide, respectively. In Fig. 5 the positions of the original and optimized PhC are shown. Clearly the original PhC design is away from the optimal region, with the thickness difference of 29% for Ta_2O_5 layers and only 4% for SiO_2 layers.

Figure 6(left) shows distributions of the BSW sensor parameters for both original and optimized PhCs (± 3% thickness uncertainty). The distributions are well separated and the FoM_S increase is about 8 times its uncertainty, indicating that the optimization leads to results that can be appreciated in the presence of fabrication tolerances. It is clear that the optimized sensor has enhanced characteristics. The FoM_S is about 4 times larger. This results mainly from the change of *D* and *W*, as S_S shows only a slight change. Note that the BSW resonance width is much smaller than the width measured in a case of the spectrally broad illumination (cf. Fig. 3).
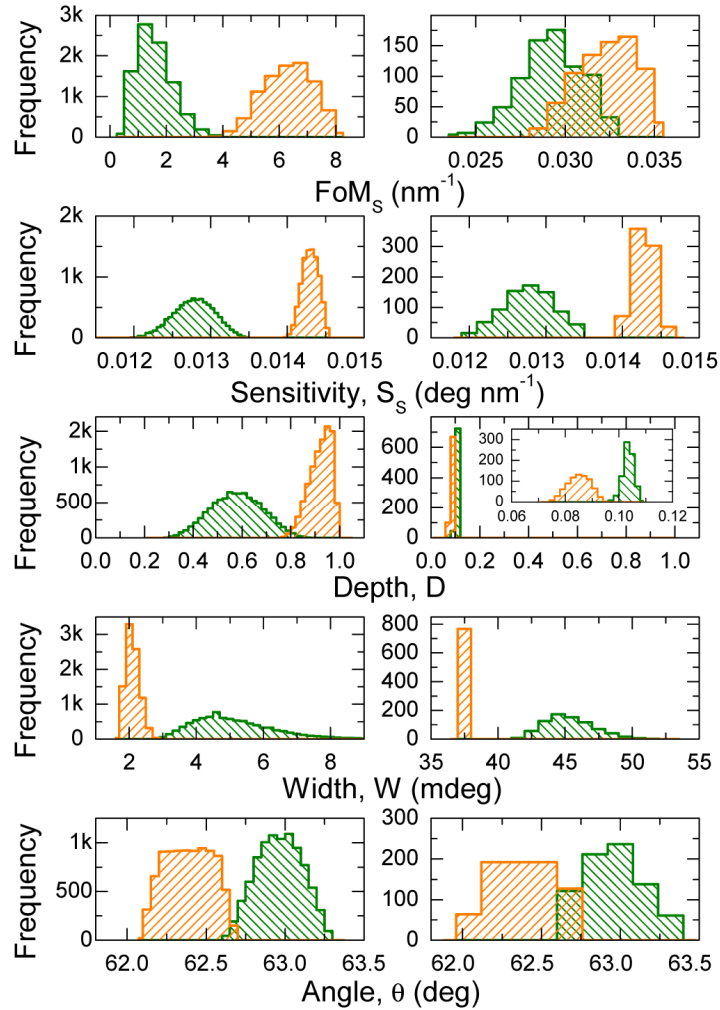
Fig. 6. Histograms of the distributions of BSW resonance angle, width, depth, sensitivity, and figure of merit at λ_0, simulated for the original (green) and optimized (red) PhC with an error of $\pm$ 3% in the layer thicknesses. (Left) Monochromatic illumination. The histograms are based on a set of 8960 sensors. (Right) Polychromatic illumination with $\Delta\lambda_0 = 2.5$ nm. The histograms are based on a set of 767 sensors.

In Table 2 we summarize the numerical values for the median and the standard deviation of the distributions of both S_V and S_S, along with those for the corresponding FoM and LoD. Table 2 could suggest that the optimized sensor, when operated in monochromatic regime, can display values as low as $LoD_V = 2.7 \times 10^{-7}$ RIU ($LoD_S = 0.54$ pm). However we have to keep in mind that such a LoD is reached only if the BSW resonances can be sampled by the CCD. In the present case, the BSW resonance width is $W = (4.95 \pm 1.23)$ mdeg and cannot be sampled properly by 1280 pixel CCD with $A = 4$ deg. The only way to sample the resonance is then to reduce the angular range down to the minimum permitted by the robustness criteria, i.e. $A = 0.9$ deg. Under such conditions, according to the Eq. (1), the limit can get as low as $LoD_V = 1.3 \times 10^{-7}$ RIU ($LoD_S = 0.26$ pm) and the resonance would be sampled with about 7 pixels. Of course a CCD camera with a large number of pixels can also be used and lead to further improvement.

As far as robustness is concerned, the relative uncertainty (σ/μ) of the FoM reduces significantly from about 40% to 10%. It is noteworthy that the FoM standard deviation could

not be evaluated directly from the standard deviations of W, D, and S, because of the mutual dependence between them. It is important that the relative uncertainty of the LoD, which is calculated with a fixed angular range of 4 deg and $N = 1280$ pixels, is decreased by the optimization, down to less than 10% form more than 30%.

The resonance angle distribution of the optimized design has the same uncertainty σ_θ as the original design, despite the distribution become flat around its median value. The uncertainty of S_V, and therefore the uncertainty of the angular dynamic range (see Eq. (8)), for the optimized sensor is very similar to the uncertainty of the original sensor, even though the median value of S_V is larger for the optimized sensor.

Considering the uncertainties of the resonance angle, dynamic range, and the reduced uncertainty of the LoD, and applying the criteria given in Eqs. (4), (8), and (9), we conclude that the optimized BSW sensor is more robust than the original design.

Finally, we note that there is a visible difference between the relative uncertainties of S_V and S_S, cf. $(\sigma/\mu)_{Sv} > 4\%$ and $(\sigma/\mu)_{Ss} < 1\%$ for the optimized device. This difference is a result of the different angular dependencies of S_V and S_S (see the Eq. (3)), which is more noticeable for the optimized sensor because its resonance angle is closer to the critical angle.

Figure 6(right) shows distributions of the BSW sensor parameters for both original and optimized PhCs (± 3% thickness uncertainty), calculated for a polychromatic illumination with $\Delta\lambda_0 = 2.5$ nm. The histograms show that optimization does not lead to a marked improvement of W and D, as these are strongly affected by the illumination spectral width. The improvement of S_S is similar to that found for the monochromatic case. As a result the distributions of the FoM$_S$ for the optimized and original designs are not well separated and a poor improvement (25%) of the median FoM is found. Comparison of the distributions found for W and D in the two cases supports our observation that, for broad resonances, a larger σ_W gives rise to a smaller σ_D, as it has been already discussed above (Fig. 3).

Table 2. Summary of the key parameters for the original and optimized BSW sensors in a case of the monochromatic illumination at λ_0

Figure		Units	Original device			Optimized device		
			μ	σ	σ / μ [%]	μ	σ	σ / μ [%]
θ		deg	62.96	0.15	0.24	62.39	0.15	0.25
S_V		deg / RIU	22.2	1.0	4.5	28.2	1.3	4.6
S_S		mdeg / nm	12.8	0.27	2.1	14.3	0.11	0.8
FoM	Volume	RIU^{-1}	2640	1070	40.5	12700	1400	11.0
	Surface	nm^{-1}	1.50	0.63	42.1	6.33	0.85	13.4
LoD	Volume	10^{-6} RIU	0.85	0.29	33.9	0.27	0.02	7.0
	Surface	pm	1.49	0.53	35.6	0.54	0.05	9.2

In Table 3 we summarize the numerical values for the median and the standard deviation of the distributions of both S_V and S_S, along with those for the corresponding FoM and LoD. The optimized design leads to a limit of detection that at minimum can take the value LoD$_V$ = 1.26×10^{-5} RIU or LoD$_S$ = 25 pm. Again one can reduce such a limit by sampling a smaller angular range. For $A = 0.9$ deg one can get to LoD$_V$ = 5.7×10^{-6} RIU.

Table 3. Summary of the key parameters for the original and optimized BSW sensors in a case of illumination with the light source having 2.5 nm bandwidth centered at λ_0

Figure		Units	Original device			Optimized device		
			μ	σ	σ / μ [%]	μ	σ	σ / μ [%]
θ		deg	62.96	0.18	0.28	62.38	0.18	0.29
S_V		deg / RIU	22.2	1.2	5.3	28.2	1.5	5.2
S_S		mdeg / nm	12.8	0.33	2.6	14.3	0.14	1.0
FoM	Volume	RIU^{-1}	50.7	3.42	6.7	64.0	5.89	9.2
	Surface	nm^{-1}	0.029	0.0018	6.0	0.032	0.0016	5.0
LoD	Volume	10^{-6} RIU	14.5	0.82	5.6	12.6	1.17	9.2
	Surface	pm	25.2	1.12	4.4	24.9	1.27	5.1

In order to clarify to the origin of the improvement of the robustness when optimizing the PhC design we calculated the photonic band-edges and the location of the BSW states for a range of PhC designs. In Fig. 7 we show the calculations performed for monochromatic illumination at λ_0, corresponding to a constant value $\omega_0 = 2\pi c/\lambda_0 = 2.34 \times 10^{15}$ rad/s marked with a green line in the plot. For each value of the fill factor, defined as $f = d_L / (d_L + d_H)$, we calculated the transverse component of the BSW k-vector along the PhC surface and for such k-value the frequencies of the light-line (blue), upper band edge (green) and lower band edge (orange). The frequencies were calculated by means of an iterative plane wave eigen-solver method [34]. The original design corresponds to $f = 0.744$, whereas the optimized design corresponds to $f = 0.810$. When varying the thicknesses of the PhC layers in the same range used in Fig. 5 (about 40%), the light line, upper, and lower band edge frequencies span the regions filled with blue, green and orange colors in Fig. 7, respectively. The small white regions inside the colored ones correspond to the domains explored for a $\pm$ 3% thickness variation and lay around the average positions of the three frequencies.
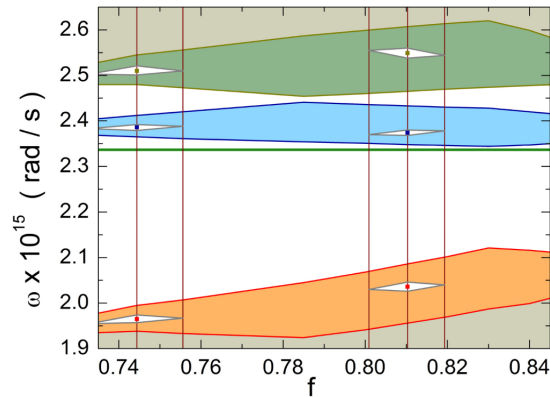

Fig. 7. Photonic band gap as a function of the fill factor, $f = d_L / (d_L + d_H)$. The PBG is calculated at the wave vector that corresponds to the BSW with a fixed frequency (green line). $f = 0.744$ and $f = 0.81$ for the non-optimized and optimized PhC, respectively. The white rhombic areas show variations in the photonic band edges and the light line that correspond to $\pm$ 3% variations in the PhC layer thicknesses (Fig. 5). The large shaded areas correspond to the thickness optimization domain. The PhC mode continuum is shown as grey areas.

The analysis of Fig. 7 leads to the following results. The ± 3% thickness variation leads to a less than ± 5% change of the PBG, in agreement with the threshold criterion given in [14] and discussed in the introduction, confirming that the PBG itself is robust with respect to fabrication tolerances. The distance of the BSW state from the upper band edge frequency is larger for the optimized design (41 ± 2)% with respect to the original design (31 ± 2)%. As a result of the larger energy spacing the optimized BSW sensor is more robust with respect to thickness and band edge variations.

Conclusions

BSW based surface wave sensors can lead to improved performance when comparing with the SPR counterparts [24, 32]. But the fabrication requires one to prepare dielectric stacks with many parameters exhibiting tolerances. The effect of such tolerances has been analyzed experimentally. Numerical simulations assuming independent thickness variations of all layers in the stack have been performed for comparison.

We found a good agreement between experimental and simulated distributions of BSW resonance angle, depth and width. The multilayer deposition with layers' thickness tolerance of ± 3% results in less than 0.3% relative error of the BSW resonance angle. This guarantees that the fabrication technology produces sensors that fit to the angular window of the optical reading system, even for small angular ranges.

The results show that optimization of the BSW sensor leads to a small improvement of the performance, in terms of LoD for example, if polychromatic illumination is used.

The results also show that monochromatic illumination enables one to achieve, for the present PhC design, the performance required for practical biosensing applications [35]. For the optimized sensors the limit of detection becomes $LoD_V = 1.3 \times 10^{-7}$ RIU ($LoD_S = 0.26$ pm) for an angular detection window of $A = 0.9$ deg. The limit of detection of not optimized sensors suffers of a large uncertainty (e.g., $(\sigma/\mu)_{LoD_V} = 34\%$). Therefore, even if a given sensor operates in the correct angular window, it could show a LoD_V that is far from the design value. Layers thickness optimization will improve the LoD_V and significantly reduce its relative uncertainty (7%), too. This indicates that batches of optimized sensors show small performance variations and can be used safely in high throughput sensing applications.

A deeper analysis indicates that the improved robustness of the optimized PhC is to be attributed to BSW states lying deeper in the photonic band gap.

Acknowledgments